

Beyond Developable: Computational Design and Fabrication with Auxetic Materials

Mina Konaković
EPFL

Keenan Crane
CMU

Bailin Deng
University of Hull

Sofien Bouaziz
EPFL

Daniel Piker

Mark Pauly
EPFL



Figure 1: Introducing a regular pattern of slits turns inextensible, but flexible sheet material into an auxetic material that can locally expand in an approximately uniform way. This modified deformation behavior allows the material to assume complex double-curved shapes. The shoe model has been fabricated from a single piece of metallic material using a new interactive rationalization method based on conformal geometry and global, non-linear optimization. Thanks to our global approach, the 2D layout of the material can be computed such that no discontinuities occur at the seam. The center zoom shows the region of the seam, where one row of triangles is doubled to allow for easy gluing along the boundaries. The base is 3D printed.

Abstract

We present a computational method for interactive 3D design and rationalization of surfaces via *auxetic* materials, i.e., flat flexible material that can stretch uniformly up to a certain extent. A key motivation for studying such material is that one can approximate doubly-curved surfaces (such as the sphere) using only flat pieces, making it attractive for fabrication. We physically realize surfaces by introducing cuts into approximately inextensible material such as sheet metal, plastic, or leather. The cutting pattern is modeled as a regular triangular linkage that yields hexagonal openings of spatially-varying radius when stretched. In the same way that isometry is fundamental to modeling developable surfaces, we leverage *conformal* geometry to understand auxetic design. In particular, we compute a global conformal map with bounded scale factor to initialize an otherwise intractable non-linear optimization. We demonstrate that this global approach can handle non-trivial topology and non-local dependencies inherent in auxetic material. Design studies and physical prototypes are used to illustrate a wide range of possible applications.

Keywords: digital fabrication, computational design, global optimization, differential geometry, conformal mapping

Concepts: •Computing methodologies → Shape modeling;

Permission to make digital or hard copies of all or part of this work for personal or classroom use is granted without fee provided that copies are not made or distributed for profit or commercial advantage and that copies bear this notice and the full citation on the first page. Copyrights for components of this work owned by others than the author(s) must be honored. Abstracting with credit is permitted. To copy otherwise, or republish, to post on servers or to redistribute to lists, requires prior specific permission and/or a fee. Request permissions from permissions@acm.org. © 2016 Copyright held by the owner/author(s). Publication rights licensed to ACM.

1 Introduction

Recent advances in material science and digital fabrication provide promising opportunities for industrial and product design, engineering, architecture, art and science [Caneparo 2014; Gibson et al. 2015]. To bring these innovations to fruition, effective computational tools are needed that link creative design exploration to material realization. A versatile approach is to abstract material and fabrication constraints into suitable *geometric* representations which are more readily translated into numerical algorithms. Successful examples of this approach include developable surface approximation targeting material such as paper, thin wood or metal [Kilian et al. 2008; Tang et al. 2016], conical and circular meshes for architectural facades [Liu et al. 2006], and Chebyshev nets for cloth and wire mesh materials [Garg et al. 2014].

In this paper we study approximation of surfaces by near-inextensible material (such as sheet metal or plastic) cut along a regular pattern of thin slits (see Figure 2). Elements formed through this cutting process can rotate relative to their neighbors, allowing the surface to stretch uniformly up to a certain limit. This stretching in turn allows the surface to exhibit non-zero Gaussian curvature, thus enriching the space of possible shapes relative to traditional developable design. We call such patterns *auxetic linkages*—the term *auxetic* refers to solid materials with negative Poisson ratio [Evans and Alderson 2000], a behavior that our augmented materials exhibit at the macro scale.

For computational design, we use constraint-based optimization to find configurations that closely approximate a target surface. A key insight is that one can leverage theory and algorithms from

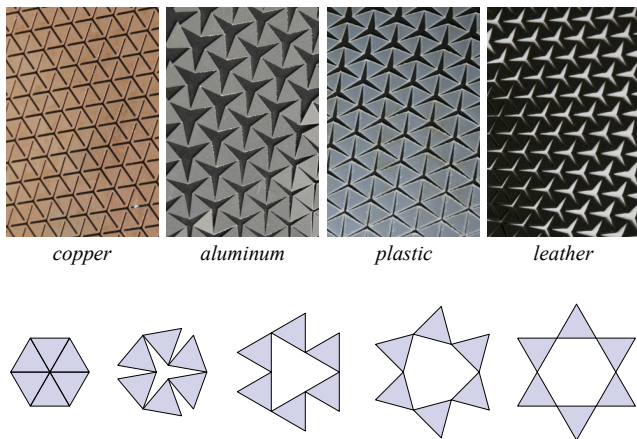


Figure 2: Top: Samples of materials used in our experiments. The leftmost photo shows the undeformed configuration. Bottom: Geometric abstraction using a triangular linkage. A single unit of the linkage deforms to form a regular hexagon opening in the maximally extended configuration.

conformal geometry to facilitate the design process. In particular, conformal maps with *bounded scale factor* provide highly effective initialization for our non-linear solver—initialization is often the most difficult step in computational rationalization [Pottmann et al. 2015]. Global optimization also helps address challenging design decisions—for instance, prediction of the 2D region that most easily approximates a target shape in 3D (see for example Figure 1). Here, global rigidity makes a manual, incremental design approach ineffective, i.e., simply wrapping a piece of material around a target object is unlikely to succeed (see Figure 11), since the shape of the boundary strongly influences the space of feasible configurations (Appendix A). Moreover, it is nearly impossible to predict (by hand) how material should be cut and oriented to achieve global continuity across seams. Computation also aids the constrained exploration of *cone singularities*, essential for surfaces with large Gaussian curvature.

Through a series of design studies and physical prototypes we demonstrate that our solution encompasses a rich class of shapes, with attractive material and functional properties. This approach opens up new design opportunities in diverse fields, including biomechanics, engineering, consumer goods, and architecture; it also inspires new fundamental questions in discrete differential geometry.

2 Related Work

Material-aware computational design. Various computational tools assist the design of 3D shapes that are realized using specific physical materials. Typically, these materials impose fabrication or assembly requirements that are incorporated as geometric constraints. For example, Igarashi et al. [2012] model 3D beadwork as polygonal meshes with near-uniform edge length, while Garg et al. [2014] use Chebyshev nets to capture the deformation behavior of interwoven, inextensible wires. Similar tools have been applied to other construction techniques, including curved folding [Kilian et al. 2008; Tang et al. 2016], reciprocal frames [Song et al. 2013], inflatable structures [Skouras et al. 2014], Zometool [Zimmer and Kobbelt 2014], wire wrapping [Iarussi et al. 2015], flexible rod meshes [Pérez et al. 2015], LEGO [Testuz et al. 2013; Luo et al. 2015], and intersecting planar pieces [Hildebrand et al. 2012; Schwartzburg and Pauly 2013; Cignoni et al. 2014]. Our approach extends this line of inquiry, focusing on a new class of material behavior obtained

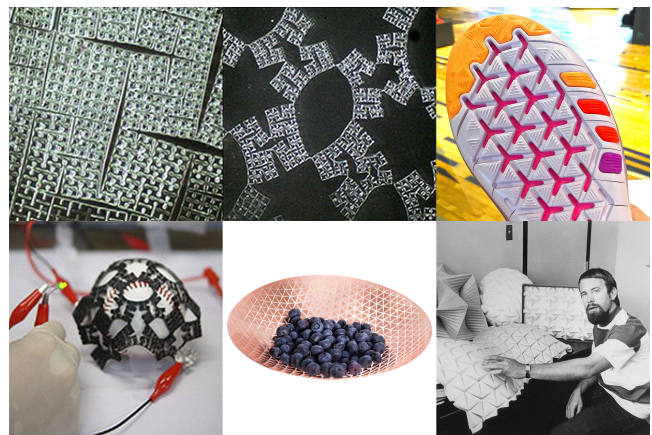


Figure 3: (Top to bottom, left to right:) Regular patterns have been used to emulate auxetic behavior in microscopic materials, footwear, electronically actuated materials, simple design applications, and origami (image courtesy of Yigil Cho et al., fundamental.berlin, and Eric Gjerde). To date, however, these applications have been limited to very simple geometries (e.g., planar or spherical) due to the lack of sophisticated design tools.

by cutting otherwise inextensible sheets. We therefore encounter a unique set of geometric constraints, demanding a new computational approach.

Origami. The cut pattern we study has been used by Ron Resch in the context of origami design [Resch 1973] (see Figure 3, bottom right). Tachi [2010] further studied this pattern and introduced various extensions for origami design [Tachi 2013]. Building on earlier work on freeform origami, he presents an optimization method to realize double-curved origami surfaces by solving a series of constraints derived from the specific origami folding method. Note that this construction is inherently more constrained due to the absence of gaps in the pattern.

Material science. Physical realizations of the cutting pattern we use in our work also appear in design objects (Figure 3, bottom middle). In this specific piece a circular shape with fixed boundary can be manually deformed into simple shapes such as a bowl. Kim and co-workers [2012] create a new self-actuating material by photo-patterning polymer films that exhibits approximately conformal deformation behavior under temperature changes. They show simulation results where initially flat material assumes simple shapes such as spherical caps, cones, or basic minimal surfaces. Cho et al. [2014] and Gatt et al. [2015] report that hierarchical cut patterns similar to our linkages can drastically increase the expandability of thin sheet materials. Moreover, Cho et al. show in their simulation that such cut patterns allow the material to be wrapped onto simple 3D shapes such as spheres and cubes using a conformal deformation. Very recently, Rafsanjani and Pasini [2016] demonstrate the use of auxetic materials to achieve reversible reconfiguration between two stable arrangements of geometric patterns. Our work not only provides geometrical insights into these phenomena, but also shows that through a carefully designed optimization we can realize a much broader class of surface shapes with auxetic materials.

Conformal mapping. We briefly review the literature on computing angle-preserving or *conformal* maps, which play a crucial role in the initialization of our solver—for a more extensive discussion, see Gu & Yau [2008]. In computer graphics, conformal



Figure 4: While several design and engineering applications have used the kagome lattice, they have been so far restricted to very simple geometries like the hemisphere. In contrast, we can approximate arbitrary curved surfaces by an auxetic linkage—here we show two configurations of an identical linkage, opening the door to reconfigurable matter.

maps are often associated with texture mapping [Lévy et al. 2002]; more broadly they play a role in a diverse array of computational applications including simulation [Bazant and Crowdy 2005], shape analysis [Ben-Chen and Gotsman 2008; Lipman and Funkhouser 2009], surface fairing [Crane et al. 2013], shape editing [Crane et al. 2011; Vaxman et al. 2015], and layout of sensor networks [Li et al. 2013]. In architectural geometry, conformal maps have been used for designing circle and sphere packings [Schiftner et al. 2009] and paneling layouts [Röhrig et al. 2014] on freeform surfaces.

A variety of strategies have been proposed to numerically approximate conformal maps based on different characterizations in the smooth setting. These include piecewise linear discretization of the Cauchy-Riemann equations [Lévy et al. 2002; Desbrun et al. 2002], conformal gradient fields [Gu and Yau 2003], circle packings [Stephenson 2003; Guo 2011], circle patterns [Kharevych et al. 2006], spin transformations [Crane et al. 2011], and local Möbius transformations [Vaxman et al. 2015]. Most relevant to our setting are methods based on conformal scaling of the metric [Springborn et al. 2008; Ben-Chen et al. 2008], which provide additional flexibility via the insertion of *cone singularities* (Section 3.2). *Quasiconformal* methods allow for maps with bounded angle distortion [Weber et al. 2012; Lipman 2012]. In contrast, we seek maps with *scale factors* bounded to a predefined range. None of the work above directly enforces such bounds. Aflalo et al. [2013] optimize conformal maps to make scaling as uniform as possible, providing a theoretical bound on the resulting scale factor. However, this bound can be much larger than our feasible range, making the method unsuitable for our problem.

3 Auxetic Linkages

The auxetic behavior of our surfaces results from cutting slits into the material in a specific pattern illustrated in Figure 2. When experimenting with different material samples we observed that under deformation, the triangles remain close to rigid. The deformation is concentrated at the hinge points connecting the triangles as these offer the least resistance to the exerted forces. We also noted that the openings that form remain roughly isotropic and that their shape

varies smoothly over the surface. This indicates that locally the surface scales approximately uniformly without significant shearing.

We geometrically abstract the cutting pattern by a kinematic linkage composed of equilateral triangles arranged in a regular lattice. Each triangle is connected to three adjacent triangles at hinge vertices. When stretching the surface, triangles can rotate around the hinges relative to their neighbors, forming hexahedral openings. These triangle rotations are coupled. For example, in an infinite planar lattice, one can see through a counting argument that there is only a single degree of freedom in the entire linkage that allows for a global uniform scaling. If a planar linkage has a boundary, however, we obtain one degree of freedom per degree-2 boundary vertex (see also Section 3.3 and Appendix A for more details).

In the completely open configuration, i.e., when stretching the material maximally, the triangles and openings form a trihexagonal pattern, also known as the Kagome lattice. In this configuration, the surface area of the material including the openings is four times larger than in the fully closed configuration.

Our observation of locally uniform scaling under deformation of the linkage surface provides a direct link to conformal geometry. More specifically, we can exploit the theory and algorithms of conformal maps to find a globally consistent initialization for a subsequent non-linear optimization that maps a closed 2D linkage to a given 3D design surface.

3.1 Conformal Geometry

One attractive feature of conformal geometry is that the curvature of a surface is easily expressed using the logarithmic factor (whereas in general, the expression can be rather complicated). We take advantage of this relationship to help reason about our design process.

In particular, let $\Omega \subset \mathbb{R}^2$ be any region in the complex plane, and consider a map $f : \Omega \rightarrow \mathbb{R}^3$ that gives Ω some new (e.g., curved) geometry. Let df denote the Jacobian or *differential* of f , expressing how a vector in \mathbb{R}^2 gets transformed by f as we go into \mathbb{R}^3 . If the inner products $X \cdot Y$ and $df(X) \cdot df(Y)$ differ only up to a positive rescaling λ at each point, then we say that f is *conformal*. Geometrically, then, we know that conformal maps must preserve *angles*, since angles can be expressed in terms of the inner product. The fact that λ is *positive* ensures that it never passes through zero, i.e., angles are always well-defined.

Often it will be convenient to express the conformal scale factor $\lambda : \Omega \rightarrow \mathbb{R}^+$ as $\lambda = e^\phi$, since now ϕ can be *any* function $\phi : \Omega \rightarrow \mathbb{R}$ (i.e., not just a positive one); ϕ is called the *logarithmic scale factor*, since $\phi = \log(\lambda)$. From here, the *Gaussian curvature* K of the target surface $f(\Omega)$ can be expressed as

$$K = \frac{\Delta \phi}{e^{2\phi}} = \Delta_f \phi, \quad (1)$$

where Δ denotes the Laplace operator in the plane [Ben-Chen et al. 2008], and Δ_f denotes the Laplace-Beltrami operator on the new surface. Notice that for conformal maps from the plane to itself ($K = 0$), ϕ is a harmonic function, i.e. $\Delta \phi = 0$.

3.1.1 Bounded Scaling

In principle, the Riemann mapping theorem guarantees that every surface of disk topology can be realized via a conformal map f . For auxetic design, however, we must restrict our search to conformal maps where the scale factor λ is bounded between 1 and some constant $\sigma > 1$. (Note that this condition is different from *quasiconformality*, which puts bounds on *angle* distortion.) These bounds

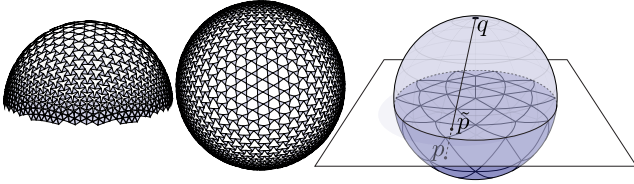


Figure 5: Conformal mapping of the sphere using the stereographic projection sketched on the right. Since our linkage pattern restricts the conformal factor to be less or equal to two, at most a half-sphere can be realized with a single regular patch of auxetic material. Note how the surface is completely closed at the boundary and maximally stretched in the center.

on the conformal factor imply that not every surface can be approximated (at least, not without additional *cone singularities*—see Section 3.2).

An idealized version of our linkage can at most double in size ($\sigma = 2$). To see why, consider Figure 2, bottom: each vertex in the closed configuration becomes an empty hexagon in the fully extended configuration. Hence, if the area of each triangle is 1, then we go from a total area of F to $F + 6V$, where V and F are the number of vertices and faces in the pattern, respectively. But since the ratio of faces to vertices in the closed pattern is $2 : 1$, the final area is $2V + 6V = 8V$ for an expansion factor of $8V/2V = 4$ in area, or $\sqrt{4} = 2$ in length. For physical realizations, σ must be strictly smaller than the ideal value since the material undergoes significant deformations at hinge points which can lead to material failure. For materials tested in our experiments, appropriate values of σ were determined empirically (see Section 5).

These restrictions lead to a natural question: are auxetic materials with bounded scale flexible enough to approximate interesting geometry? To provide some intuition about this question, we consider two simple examples below.

Surjectivity. A conformal parameterization of the sphere S^2 can be obtained via *stereographic projection* [Feeman 2002]: each point $p \in S^2$ is projected to a point \tilde{p} on the equatorial plane by finding the intersection with a segment that connects p to the north pole q . The area element induced by f is $d\tilde{A} := 4/(1 + |\tilde{p}|^2)^2 dA$, where dA is the usual area on the plane. This means that the length scale factor is 2 at the origin, shrinks to 1 at the equator, and for points outside the unit disk it shrinks further, to arbitrarily small values. Moreover, stereographic projection is the conformal parameterization of the hemisphere with *least* area distortion, because it is an isometry along the boundary [Springborn et al. 2008, Appendix E]. Therefore, a single auxetic patch can cover *at most* half of the sphere when the maximal conformal factor is bounded by 2, i.e. local area increase is bounded by a factor 4 (see Figure 5).

Integrability. Independent of the scale bound, there is also a question of *integrability*: is it possible to approximate surfaces that close up seamlessly? Following [Sullivan 2011], we consider a family of conformal embeddings of the torus $f_s(u, v) : [0, s] \times [0, 1] \rightarrow R^3$ given by

$$f_s(u, v) = \frac{t + 1}{2\pi(t - \cos(2\pi v))} \begin{pmatrix} s \cos(2\pi u/s) \\ s \sin(2\pi u/s) \\ \sin(2\pi v) \end{pmatrix},$$

where $t = \sqrt{s^2 + 1} = R/r$ is the ratio of major radius R to minor radius r . A simple calculation reveals that this mapping has minimal

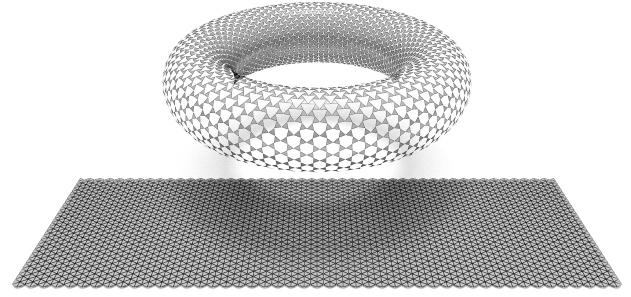


Figure 6: The linkage we study can even be used to construct closed surfaces with nontrivial topology. Here a torus with rectangular conformal type floats over its initial (closed) tiling, given by the fundamental domain; the aspect ratio of this rectangle maximizes the relative scaling that can be achieved with our linkage.

scaling factor of one, and maximal scaling factor given by $\sigma = \frac{t+1}{t-1}$. Since our tiling pattern restricts σ to be below two, this leads to the constraint $t > 3$ (see Figure 6). This restriction again motivates the need for cone singularities, which provide additional flexibility.

3.2 Cone Singularities

A surface has a *cone metric* if it can be perfectly flattened away from a collection of isolated points called *cone singularities*—examples include the paper cups used for snow cones (one cone) and cone coffee filters (two cones). Cutting from the boundary to each cone point yields a surface that can be flattened without any stretching. In recent years, cone singularities have been adopted as a tool for conformal surface parameterization: rather than mapping directly to the plane, one computes a conformal map to a cone metric, which can then be trivially flattened (via cutting) [Kharevych et al. 2006; Springborn et al. 2008; Ben-Chen et al. 2008]. The key benefit of concentrating curvature at cones is that area distortion is *also* concentrated near cones (see Equation (1)). For texture mapping, controlled area distortion improves signal fidelity; for auxetic design, it is crucial for approximating surfaces with large Gaussian curvature. However, we face additional challenges due to the discrete, rigid nature of our linkage.

In our linkage, cone singularities correspond to vertices of irregular degree. Recall that the *angle defect* at a vertex in a standard triangle mesh is 2π minus the sum of incident angles; a vertex can be flattened only if this value is equal to zero. In general, the angle defect is equal to the integrated *Gaussian curvature* in a small neighborhood

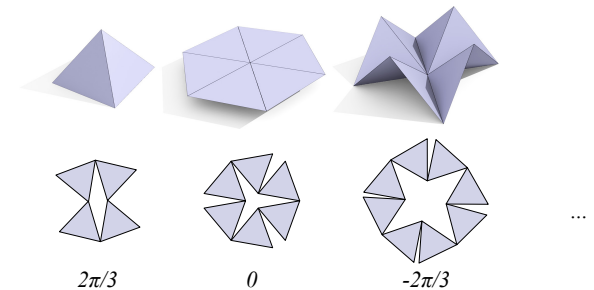


Figure 7: Incorporating irregular vertices or cone singularities into our linkage pattern allows us to better approximate surfaces with large Gaussian curvature. Since each vertex must have even degree, the possible cone angles come in quanta of $2\pi/3$. Top: closed configuration. Bottom: corresponding open pattern.

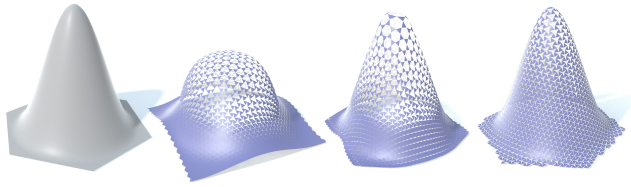


Figure 8: Without singularities, rationalizing a bump with large curvature (left) results in either large deviation from the target surface (center left) or nonrigid distortion of triangles (center right). Adding a cone singularity at the tip allows one to closely approximate the target surface while satisfying fabrication constraints (right).

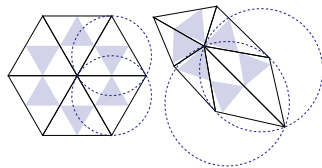
around the vertex. Suppose, then, that we generalize our closed pattern from a regular grid to an equilateral triangle mesh where every vertex has even degree. At each vertex, the corresponding open pattern is obtained by cutting along every other edge *almost* to the opposite vertex (see Figure 7). Globally, these cuts are made in such a way that no edge is cut twice; note that there are always two possible cutting patterns. Since every triangle is equilateral, and every vertex has even degree, the angle defect at each vertex is $2\pi - 2k\pi/3$ for some integer $k \geq 0$. Typically we find that cones of curvature $\pm 2\pi/3$ are the most useful, since cones with larger (negative) curvature will induce more severe area distortion.

Although irregular vertices globally reduce area distortion (moving us toward the bound $\lambda < \sigma$ from Section 3.1), they also incur large area distortion in the immediate vicinity of the cone. In the smooth setting, in fact, the scale factor goes to *infinity*, since ϕ locally looks like a harmonic Green’s function $\frac{1}{2\pi} \log r$, where r is the distance from the cone; in the discrete setting the situation is not quite as dire, since this area distortion is distributed over a finite region. However, high curvature at cones still presents some difficulty. For example, Figure 9 shows an illustration where a subdivided octahedral linkage cannot be deformed into a round sphere without either creating spikes or self-intersections. A practical remedy is to remove triangles near the cone, creating additional openings in the surface at the cost of leaving some triangles “dangling,” i.e., connected to only two neighbors. Despite these limitations, cone singularities significantly increase the space of shapes that are well-approximated by a single patch of material (see also Section 5).

Figure 8 validates the necessity of cone singularities in auxetic linkage design. For the target bump surface, conformal parameterization without singularities results in out-of-bound scale factors around the tip of the bump. Starting from such parameterization, the optimized linkage either deviates from the target surface or has non-uniform edge length. In contrast, introducing a cone singularity at the tip enables close approximation of the target surface, while satisfying all the constraints (see Section 4 for details).

3.3 Discrete Conformal Geometry

Although conformal geometry provides us with a great deal of intuition, we have thus far shown no rigorous, formal connection between our linkage and existing conformal theory. Naturally one would like to



connect this discrete linkage to discrete theories such as *circle patterns* [Kharevych et al. 2006] or *discrete conformal equivalence* [Springborn et al. 2008]; so far, however, such a connection remains elusive. For instance, if one inscribes our linkage in a triangulation, one can easily construct configurations where this

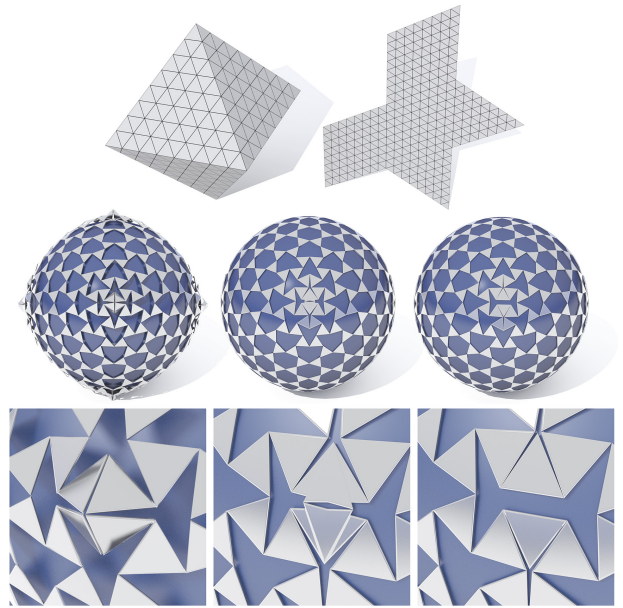


Figure 9: The discrete, rigid nature of auxetic linkages introduces additional challenges for cone singularities. Here, six singularities on the octahedron (of curvature $2\pi/3$) cannot be flattened to match the curvature of the sphere without violating our maximal stretching criterion elsewhere on the surface. Hence we obtain high-curvature spikes (left) or self-intersections (middle) that can be avoided by deleting triangles (right) at the expense of creating dangling triangles only connected to two neighbors.

triangulation has neither the same length cross ratios nor the same angle sums as an equilateral grid (see inset). One can, however, establish one key fact that is strongly suggestive of a conformal theory, namely that the configuration of a finite planar linkage is determined by *real* degrees of freedom at the boundary (see Appendix A). This situation corresponds to Cauchy-Riemann, where one cannot prescribe the full boundary values of a conformal map, but rather only one of its two real components. This fact places our linkage between rigid mechanisms like scissor-jointed structures, which have only one global degree of freedom, and far more flexible discrete harmonic maps, which have one *vector-valued* degree of freedom per boundary vertex. Understanding the geometric meaning of these boundary values, and indeed, further connections to conformal geometry is an enticing direction for future study. A particularly compelling feature of auxetic linkages is that each unit can rotate either clockwise or counter-clockwise, potentially capturing the behavior of both holomorphic and *antiholomorphic* functions.

4 Surface Rationalization

The central problem that we address in this paper is surface rationalization, i.e., how to approximate a given 3D design surface with the linkage-based auxetic material introduced above. The highly non-local nature of the problem resulting from the spatial coupling of triangles imposed by our specific linkage topology, calls for a global approach using numerical optimization. At the same time, it is essential to keep the designer in the loop, as many high-level aesthetic decisions about the specific surface layout require user guidance. We therefore propose an interactive, optimization-supported rationalization approach described in the remainder of this section.

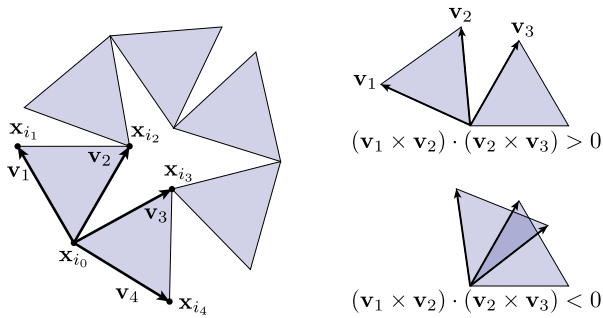


Figure 10: Non-penetration constraint. Viewed from the normal direction of the triangle $\mathbf{v}_1\mathbf{v}_2$ (shown on the right), the condition $(\mathbf{v}_1 \times \mathbf{v}_2) \cdot (\mathbf{v}_2 \times \mathbf{v}_3) \geq 0$ prevents \mathbf{v}_3 from projecting into the interior of the triangle $\mathbf{v}_1\mathbf{v}_2$.

4.1 Interactive Workflow

Based on the connection between auxetic linkages and conformal maps outlined above, we introduce the following workflow for rationalization: We first create a conformal mapping of the 3D input surface to the 2D plane based on the method described in [Springborn et al. 2008]¹. Since this mapping has a strong influence on the visual appearance of the final surface, we provide full control over the specific properties of the conformal map. In particular, the designer indicates the desired locations of cone singularities and marks the cutting path necessary to map the surface to a 2D patch with disk topology.

During editing, we visualize the conformal factor on the surface so that the designer can introduce additional singularities to ensure that the scale factor is below the bound mandated by the limited material extensibility. Given the conformal map, the designer selects the global orientation of the regular tiling grid, which is then clipped appropriately and lifted onto the 3D design surface.

Due to the discrete nature of our linkage, the conformally lifted pattern typically does not satisfy the rigidity constraints of triangles exactly. Furthermore, neighboring triangles can potentially interpenetrate. We therefore apply a global optimization to satisfy all constraints as described below.

The optimization also provides us with more flexibility when creating the conformal map. If the bounds on the scaling factor are violated within a confined region, the optimization can typically recover a valid solution. In general, we apply several iterations between adapting the conform map and global optimization.

4.2 Numerical Optimization

The conformal map provides us with 3D positions on the design surface for each linkage vertex. The resulting lifted linkage needs to be further optimized to satisfy the following requirements: 1) all triangles are rigid, i.e. have the same edge length prescribed by the user; 2) the triangles do not collide with each other; 3) the vertices remain close to the input design surface. To meet these objectives we minimize an objective function with respect to the vertex positions $\mathbf{x}_1, \dots, \mathbf{x}_n \in \mathbb{R}^3$ (omitted below for notational brevity):

$$E(\mathbf{x}_1, \dots, \mathbf{x}_n) = w_1 E_{\text{design}} + w_2 E_{\text{rigid}} + w_3 E_{\text{collision}}, \quad (2)$$

where E_{design} , E_{rigid} , and $E_{\text{collision}}$ measure the closeness to the design surface, the violation of rigidity constraints, and the violation of

¹available in the software tool *Varylab* at www.varylab.com

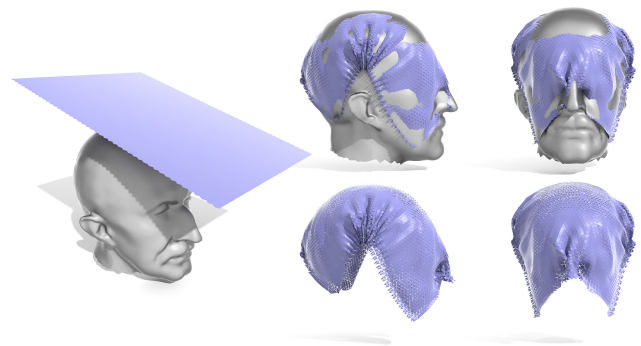


Figure 11: Optimizing auxetic linkages from arbitrary initial shapes can lead to undesirable local minima. Left: initializing a linkage as a flat rectangular patch for the rationalization of *Max Planck*. Right: undesirable foldovers and wrinkles in the optimized linkage.

non-penetration constraints, respectively. The weights w_1, w_2, w_3 control the trade-off between these objectives.

The energy terms of Equation (2) are defined according to the framework proposed by [Bouaziz et al. 2012], i.e., using projection operators onto feasible sets. Specifically,

$$E_{\text{design}} = \sum_{i=1}^n \|\mathbf{x}_i - P_{\text{design}}(\mathbf{x}_i)\|^2,$$

where $P_{\text{design}}(\mathbf{x}_i)$ is the projection of vertex \mathbf{x}_i onto the input design surface. The rigidity constraint is formulated as

$$E_{\text{rigid}} = \sum_{(i,j) \in \mathcal{E}} \|\mathbf{x}_i - \mathbf{x}_j - P_{\text{edge}}(\mathbf{x}_i - \mathbf{x}_j)\|^2,$$

where \mathcal{E} is the index set for all vertex pairs that belong to a common edge; $P_{\text{edge}}(\cdot) : \mathbb{R}^3 \mapsto \mathbb{R}^3$ is the projection operator onto the set of vectors whose norms are equal to the user-specified edge length L : $P_{\text{edge}}(\mathbf{v}) = L\mathbf{v}/\|\mathbf{v}\|$.

For collision avoidance we enforce non-penetration locally between neighboring triangles that share a vertex. Since our initial lifted surface is already close to the solution, the optimization typically leads to only moderate changes of the shape. We therefore do not prevent global collisions to avoid unnecessary computational overhead. Let $\mathbf{v}_1, \mathbf{v}_2, \mathbf{v}_3, \mathbf{v}_4$ be four edge vectors that originate from the same vertex, where $(\mathbf{v}_1, \mathbf{v}_2)$ and $(\mathbf{v}_3, \mathbf{v}_4)$ belong to two triangles, and $\mathbf{v}_2, \mathbf{v}_3$ correspond to their shared edge in the rest shape (see Figure 10). We then require that

$$(\mathbf{v}_1 \times \mathbf{v}_2) \cdot (\mathbf{v}_2 \times \mathbf{v}_3) \geq 0, \quad (3)$$

$$(\mathbf{v}_4 \times \mathbf{v}_3) \cdot (\mathbf{v}_3 \times \mathbf{v}_2) \geq 0. \quad (4)$$

Geometrically, if $\mathbf{v}_1, \mathbf{v}_2$ are linearly independent, then they span a plane P_{12} , and \mathbf{v}_2 defines a line that cuts P_{12} into two half-planes; condition $(\mathbf{v}_1 \times \mathbf{v}_2) \cdot (\mathbf{v}_2 \times \mathbf{v}_3) \geq 0$ requires that the projection of \mathbf{v}_3 falls onto a half-plane different from \mathbf{v}_1 . Viewing along the normal of triangle $\mathbf{v}_1\mathbf{v}_2$, this condition prevents \mathbf{v}_3 from moving into the triangle $\mathbf{v}_1\mathbf{v}_2$ (see Figure 10 right). The same restriction applies to \mathbf{v}_2 with respect to triangle $\mathbf{v}_3\mathbf{v}_4$, under the condition $(\mathbf{v}_4 \times \mathbf{v}_3) \cdot (\mathbf{v}_3 \times \mathbf{v}_2) \geq 0$. The two conditions combined avoid penetration between adjacent triangles. Given three vectors $\mathbf{v}_1, \mathbf{v}_2, \mathbf{v}_3$, the projection operator onto the feasible set of (3) requires solving a system of quadratic equations, and is expensive to compute. Instead

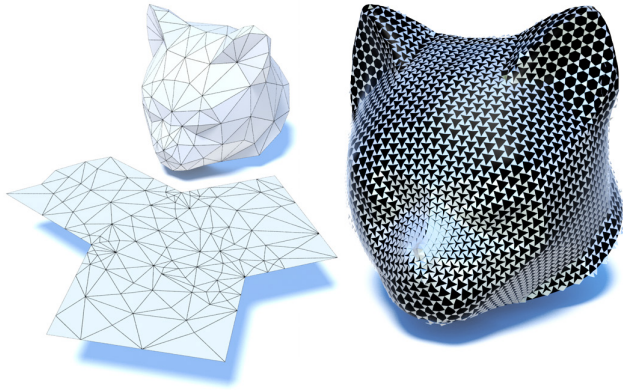


Figure 12: Rationalization of the cat model with singularities of $2\pi/3$ curvature at the nose and both ears.

we use an approximate projection operator that minimally moves $\mathbf{v}_2, \mathbf{v}_3$ to linear dependent positions if Condition (3) is violated:

$$P_{\text{collision}}([\mathbf{v}_1, \mathbf{v}_2, \mathbf{v}_3]) = \begin{cases} [\mathbf{v}_1, \mathbf{v}_2, \mathbf{v}_3] & \text{if } (\mathbf{v}_1 \times \mathbf{v}_2) \cdot (\mathbf{v}_2 \times \mathbf{v}_3) \geq 0 \\ [\mathbf{v}_1, \mathbf{h}(\mathbf{h} \cdot \mathbf{v}_2), \mathbf{h}(\mathbf{h} \cdot \mathbf{v}_3)] & \text{otherwise} \end{cases},$$

where \mathbf{h} is the left singular vector of matrix $[\mathbf{v}_2, \mathbf{v}_3] \in \mathbb{R}^{3 \times 2}$ for the largest singular value. Then the collision objective is defined as

$$E_{\text{collision}} = \sum_{\mathcal{T}} (\|[\mathbf{x}_{i_1} - \mathbf{x}_{i_0}, \mathbf{x}_{i_2} - \mathbf{x}_{i_0}, \mathbf{x}_{i_3} - \mathbf{x}_{i_0}] - P_{\text{collision}}([\mathbf{x}_{i_1} - \mathbf{x}_{i_0}, \mathbf{x}_{i_2} - \mathbf{x}_{i_0}, \mathbf{x}_{i_3} - \mathbf{x}_{i_0}])\|^2 + \|[\mathbf{x}_{i_4} - \mathbf{x}_{i_0}, \mathbf{x}_{i_3} - \mathbf{x}_{i_0}, \mathbf{x}_{i_2} - \mathbf{x}_{i_0}] - P_{\text{collision}}([\mathbf{x}_{i_4} - \mathbf{x}_{i_0}, \mathbf{x}_{i_3} - \mathbf{x}_{i_0}, \mathbf{x}_{i_2} - \mathbf{x}_{i_0}])\|^2)$$

where $\mathbf{x}_{i_0}, \mathbf{x}_{i_1}, \mathbf{x}_{i_2}, \mathbf{x}_{i_3}, \mathbf{x}_{i_4}$ are the vertex positions related to the vectors $\mathbf{v}_1, \mathbf{v}_2, \mathbf{v}_3, \mathbf{v}_4$ for a pair of neighboring triangles (see Figure 10 left), and \mathcal{T} is the index set of such vertex tuples.

Implementation details. The target function (2) is optimized using alternating minimization with auxiliary variables, as described in detail in [Bouaziz et al. 2012]. We use the open-source implementation of this method described in [Deuss et al. 2015]. The only extension necessary is the implementation of the projection operator for collisions that we provide in Appendix B.

Below we give performance data for the largest of our examples, the Max Planck model of Figure 13 with 15k vertices. All our other models have significantly fewer vertices and thus require only a fraction of the computation time. The optimization requires 2.5ms per iteration on a single core of a 2012 Macbook Pro laptop with 2.6GHz when solving for edge length and non-penetration constraints, while fixing the closest points on the design surface to the 3D positions specified by the conformal map. This is useful to get a quick first impression of the surface layout, which might inform the designer that the conformal map needs to be adapted. When solving the full optimization including dynamic closest point computations for the P_{design} projection operator, this number increases to 350ms. We typically run 20-50 iterations for visual feedback to highlight possible constraint violations that then trigger further design iterations. Once the layout is finalized we run an additional 200 iterations to obtain the final linkage surface.

The weights w_2 and w_3 in Equation (2) are kept fix at 1 for the entire optimization process. For the surface closeness weight w_1 we follow

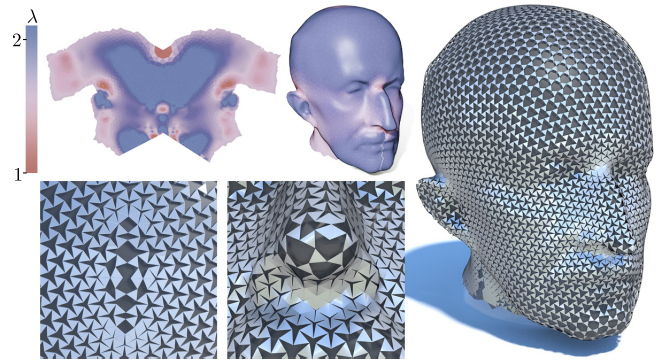


Figure 13: A rationalization of the Max Planck illustrates the limits of what can be approximated with a single patch of auxetic material. One singularity with $2\pi/3$ curvature is at the top of the nose (middle zoom) with a completely closed four-sided polygon. A combination of $2\pi/3$ and $-2\pi/3$ curvature singularities is required to close the top of the head (left zoom). The cut behind the ear could not be closed without violating the bound on the conformal factor, which is visualized on the model and 2D layout.

the relaxation strategy commonly used for non-rigid registration, see e.g. [Li et al. 2009]. We initialize w_1 with 0.001 and gradually increase its value to 0.1 to first resolve the constraints and then let the surface evolve closer towards the input design.

Our optimization problem is non-convex with many local minima, and our numerical solver only finds a local minimum close to the initial shape. Thus it is important to start the solver from a shape that is already close to the desirable solution. Our initialization using conformal maps follows a common strategy of understanding discrete objects from their continuous analogues [Pottmann et al. 2015], which proves to be effective in our experiments. In comparison, running the solver from an arbitrary initial shape often results in an undesirable local minimum (see Figure 11).

5 Applications and Physical Prototypes

We validate our computational design and rationalization approach with a number of numerical and physical experiments, illustrating the broad applicability of our approach for different materials and usage domains.

Shoe. Figure 1 shows a design of a shoe using an auxetic linkage. In contrast to a purely inextensible material, our material can realize this double curved shape with a single piece. At the same time, the pattern provides an interesting esthetic and offers certain functional properties, e.g. ventilation. Creating such a surface without optimization is extremely difficult as it is not clear how one would need to lay out the surface in 2D such that the material would match seamlessly at the cut. This highly non-local constraint is handled implicitly by our initialization based on a global conformal map.

Sculptures. In Figures 12 and 13 we show rationalizations of the cat model and the Max Planck bust, with several singularities to accommodate the complex double-curved shapes. Note how a rationalization of these surfaces with developable material would require numerous thin strips that would have to be connected along their boundaries in a way that cannot provide tangent continuity across the connections. Auxetic linkages preserve the smooth appearance of the input surface while capturing important geometric features.

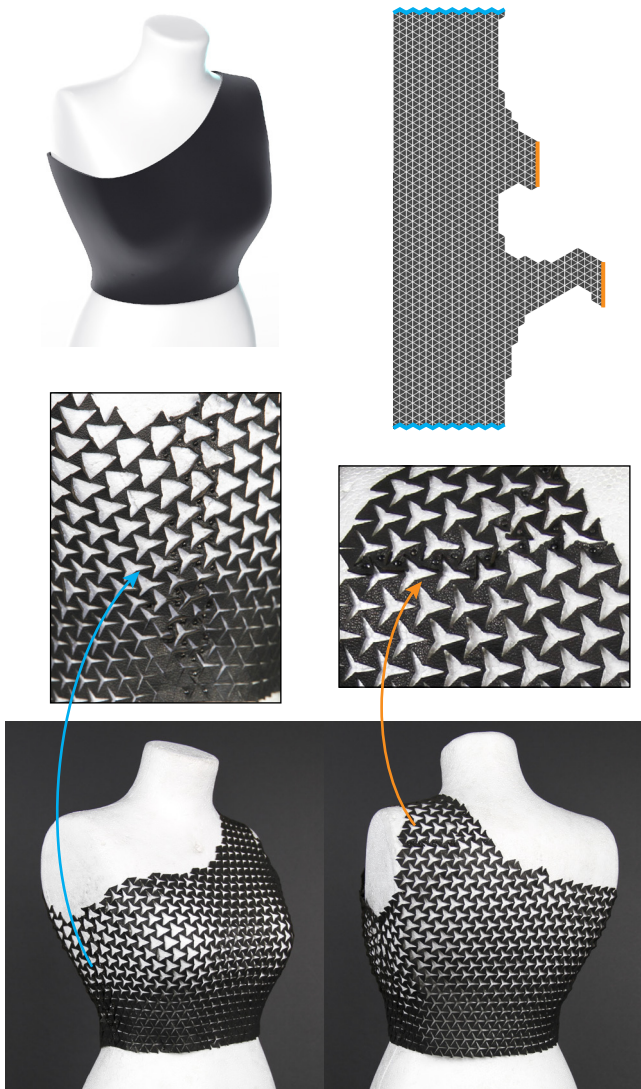


Figure 14: A double-curved top fabricated from approximately inextensible leather. The zooms illustrate the global continuity of the pattern across the seams, which are fixed with pins.

Fashion top. Figure 14 shows an application in fashion design, where auxetic material is laser cut from a nearly inextensible leather textile and stretches to conform to the doubly-curved mannequin body. Since optimization ensures a continuous transition across seams, the final dress has no visible discontinuities. The design surface was created by 3D scanning a physical mannequin, highlighting the potential of our approach for personalized fashion design.

Lamp shade. Beyond rationalization of a given input, techniques from Section 4.2 can also be used for interactive design using, e.g., a standard handle-based click-and-drag interface. Constraints on vertex positions replace the surface closeness energy in Equation (2), which is augmented with a smoothness term as described in [Bouaziz et al. 2012]. Optimization ensures that edge length and inter-penetration constraints are satisfied, allowing the user to interactively explore the shape space of a given linkage topology. Figure 16 shows an auxetic lamp shade, modeled with handle-based manipulation. The form of the object influences the emission of light, leading to interesting shadow patterns.



Figure 15: Fabrication of the Max Planck model. Top left: 3D printed reference model used for geometric guidance; Bottom left: flat, undeformed perforated copper sheet. The purple arrow indicates the singular vertex located at the tip of the nose; Middle, Right: two photographs of the final model.

Face masks. Figure 15 shows a physical realization of the Max Planck model cut from a single sheet of perforated copper. While our current fabrication technique produces a single rigid surface, kinematic linkages can also be employed in dynamic settings where an object transitions through different geometric configurations. Figure 4 illustrates this shape shifting idea, where the same linkage is used to approximate two different face models. How to mechanically actuate such a transition is an interesting question for future work.

5.1 Discussion

We empirically observed that our abstraction based on linkages of rigid elements well approximates the geometric behavior of the cut surface materials. However, we do not explicitly model the complex physical behavior at the linkage joints. Metals, for example, deform plastically to retain the deformed state, while the plastics we experimented with deform elastically and push back towards the rest state. In practice, linkage joints cannot be stretched beyond a certain limit without fracturing, which means that for many materials we cannot achieve the maximal scaling factor of the linkage. Suitable bounds need to be determined for each base material as a function of the sheet thickness and the incision depth. Currently, we determine these bounds empirically through experimentation. In general, the concrete physical behavior of each piece strongly depends on the material and the specific geometry. It would be interesting to integrate finite-element simulation into the design process to provide feedback on the structural performance of the physical realization.

For closed designs or surfaces with singularities, we currently do not optimize for the seam, but rely on the user to specify an appropriate path on the surface. While this gives the user full control, finding good cut paths is not always an easy task and additional computational support could be helpful for untrained users. Appearance of seams could be improved by quantizing the target geodesic curvature to agree with the symmetry of our triangular pattern, a la Springborn et al [2008, Section 6]; in the future, one might also consider augmented tilings that conform exactly to the boundary.

The example of Figure 16 is emblematic for applications of our method in lighting and shading control, for example, in an architectural context. Given a desired solar energy density profile, the openings and orientation of the surface can be determined through a form finding optimization, taking into account other constraints such as limits on curvature or smoothness of the facade. This is an

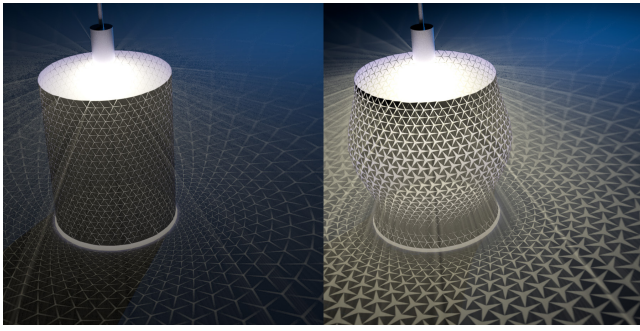


Figure 16: Our auxetic design tools can also be used to explore lighting design—here an “open” and “closed” configuration of the same linkage provide mechanical dimming.

example of the concept of form follows function (or more precisely, performance). For large scale facades, fabrication would probably follow a panel-based assembly approach, where the fact that all triangles are identical can significantly simplify manufacturing. Related to the passage of light through the material, one can also imagine other transport scenarios, e.g., flow of liquids or granular material, where the openings can be used for flow control.

6 Conclusion and Future Work

In recent years, study of isometric maps has led to numerous computational methods for geometric modeling, for example in the domains of origami, curved foldings, or developable surface rationalization. Our paper aims to initiate a similarly fruitful discussion for a richer set of surfaces that can be achieved when the material can also locally scale in a uniform way. Our results demonstrate that non-trivial shapes can be rationalized effectively, offering a new class of design surfaces with applications in many domains.

The particular cutting pattern we study here is just one of many possibilities; other regular tilings have been explored, for example in the sculptural art of Hareh Lalvani. A unified theory of linkage-based auxetic materials is an exciting avenue for future research. For example, a clear notion of discrete conformal equivalence for linkage patterns (with compatible discrete notions of curvature, Laplace operator, etc.) would provide insights into the geometry of linkage surfaces, with potential implications for algorithm design. More generally, the possibility to control the deformation behavior of sheet material by introducing cuts offers new opportunities for material-aware design. Interesting questions arise concerning the physical behavior of such materials. Form-finding algorithms and interactive design tools that optimize for the cutting pattern rather than prescribing it a priori offer a rich space for future research.

7 Acknowledgments

Thanks to Stefan Sechelmann for his valuable help with Varylab, and Alexandru Eugen Ichim for providing a face model in Figure 4. This work was supported by an NSF Mathematical Sciences Postdoctoral Research Fellowship, NSF 13-19483, and the NCCR Digital Fabrication, funded by the Swiss National Science Foundation, NCCR Digital Fabrication Agreement #51NF40-141853. In Figure 3, the Resch portrait is provided by Eric Gjerde under license *CC BY-NC 2.0*; the footwear photo was released by the authors under a Creative Commons Public Domain Dedication; other images are used with permission from David J. Srolovitz and fundamental.berlin.

References

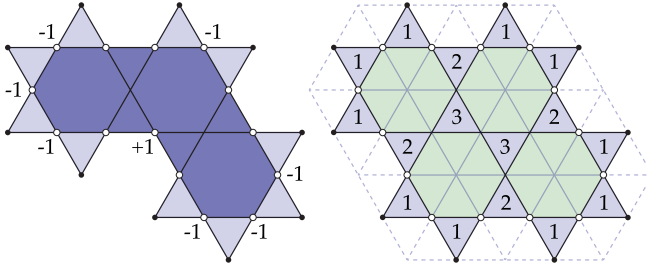
- AFLALO, Y., KIMMEL, R., AND ZIBULEVSKY, M. 2013. Conformal mapping with as uniform as possible conformal factor. *SIAM Journal on Imaging Sciences* 6, 1, 78–101.
- BAZANT, M. Z., AND CROWDY, D. 2005. *Conformal Mapping Methods for Interfacial Dynamics*.
- BEN-CHEN, M., AND GOTSMAN, C. 2008. Characterizing shape using conformal factors. In *Proceedings of the 1st Eurographics Conference on 3D Object Retrieval, 3DOR '08*, 1–8.
- BEN-CHEN, M., GOTSMAN, C., AND BUNIN, G. 2008. Conformal flattening by curvature prescription and metric scaling. *Computer Graphics Forum* 27, 2, 449–458.
- BOBENKO, A. I., AND SURIS, Y. B. 2008. *Discrete Differential Geometry: Integrable Structure*. AMS.
- BOUAZIZ, S., DEUSS, M., SCHWARTZBURG, Y., WEISE, T., AND PAULY, M. 2012. Shape-up: Shaping discrete geometry with projections. *Comput. Graph. Forum* 31, 5, 1657–1667.
- BOUAZIZ, S., MARTIN, S., LIU, T., KAVAN, L., AND PAULY, M. 2014. Projective dynamics: Fusing constraint projections for fast simulation. *ACM Trans. Graph.* 33, 4 (July), 154:1–154:11.
- CANEPARO, L. 2014. *Digital Fabrication in Architecture, Engineering and Construction*. Springer.
- CHO, Y., SHIN, J.-H., COSTA, A., KIM, T. A., KUNIN, V., LI, J., LEE, S. Y., YANG, S., HAN, H. N., CHOI, I.-S., AND SROLOVITZ, D. J. 2014. Engineering the shape and structure of materials by fractal cut. *Proceedings of the National Academy of Sciences* 111, 49, 17390–17395.
- CIGNONI, P., PIETRONI, N., MALOMO, L., AND SCOPIGNO, R. 2014. Field-aligned mesh joinery. *ACM Trans. Graph.* 33, 1 (Feb.), 11:1–11:12.
- CRANE, K., PINKALL, U., AND SCHRÖDER, P. 2011. Spin transformations of discrete surfaces. *ACM Trans. Graph.* 30, 4 (July), 104:1–104:10.
- CRANE, K., PINKALL, U., AND SCHRÖDER, P. 2013. Robust fairing via conformal curvature flow. *ACM Trans. Graph.* 32, 4 (July), 61:1–61:10.
- DESBRUN, M., MEYER, M., AND ALLIEZ, P. 2002. Intrinsic parameterizations of surface meshes. *Computer Graphics Forum* 21, 3, 209–218.
- DEUSS, M., DELEURAN, A., BOUAZIZ, S., DENG, B., PIKER, D., AND PAULY, M. 2015. ShapeOp – a robust and extensible geometric modelling paradigm. In *Modelling Behaviour*. Springer International Publishing, 505–515.
- EVANS, K. E., AND ALDERSON, A. 2000. Auxetic materials: Functional materials and structures from lateral thinking! *Advanced Materials* 12, 9, 617–628.
- FEEMAN, T. G. 2002. *Portraits of the Earth: A Mathematician Looks at Maps*. American Mathematical Society.
- GARG, A., SAGEMAN-FURNAS, A. O., DENG, B., YUE, Y., GRINSPUN, E., PAULY, M., AND WARDETZKY, M. 2014. Wire mesh design. *ACM Trans. Graph.* 33, 4 (July), 66:1–66:12.
- GATT, R., MIZZI, L., AZZOPARDI, J. I., AZZOPARDI, K. M., ATTARD, D., CASHA, A., BRIFFA, J., AND GRIMA, J. N. 2015. Hierarchical auxetic mechanical metamaterials. *Scientific Reports* 5.

- GIBSON, I., ROSEN, D., AND STUCKER, B. 2015. *Additive Manufacturing Technologies: 3D Printing, Rapid Prototyping, and Direct Digital Manufacturing*, 2nd ed. Springer.
- GU, X., AND YAU, S.-T. 2003. Global conformal surface parameterization. In *Proc. SGP*, 127–137.
- GU, X. D., AND YAU, S.-T. 2008. *Computational conformal geometry*. International Press of Boston, Inc.
- GUO, R. 2011. Local rigidity of inversive distance circle packing. *Transactions of the American Mathematical Society* 363, 9, 4757–4776.
- HILDEBRAND, K., BICKEL, B., AND ALEXA, M. 2012. crdbrd: Shape fabrication by sliding planar slices. *Computer Graphics Forum* 31, 2, 583–592.
- IARUSSI, E., LI, W., AND BOUSSEAU, A. 2015. Wrapit: Computer-assisted crafting of wire wrapped jewelry. *ACM Trans. Graph.* 34, 6 (Oct.), 221:1–221:8.
- IGARASHI, Y., IGARASHI, T., AND MITANI, J. 2012. Beady: Interactive beadwork design and construction. *ACM Trans. Graph.* 31, 4 (July), 49:1–49:9.
- KHAREVYCH, L., SPRINGBORN, B., AND SCHRÖDER, P. 2006. Discrete conformal mappings via circle patterns. *ACM Trans. Graph.* 25, 2 (Apr.), 412–438.
- KILIAN, M., FLÖRY, S., CHEN, Z., MITRA, N. J., SHEFFER, A., AND POTTMANN, H. 2008. Curved folding. *ACM Trans. Graph.* 27, 3 (Aug.), 75:1–75:9.
- KIM, J., HANNA, J. A., BYUN, M., SANTANGELO, C. D., AND HAYWARD, R. C. 2012. Designing responsive buckled surfaces by halftone gel lithography. *Science* 335, 6073 (Mar.), 1201–1205.
- LÉVY, B., PETITJEAN, S., RAY, N., AND MAILLOT, J. 2002. Least squares conformal maps for automatic texture atlas generation. *ACM Trans. Graph.* 21, 3 (July), 362–371.
- LI, H., ADAMS, B., GUIBAS, L. J., AND PAULY, M. 2009. Robust single-view geometry and motion reconstruction. *ACM Trans. Graph.* 28, 5 (Dec.), 175:1–175:10.
- LI, S., ZENG, W., ZHOU, D., GU, X. D., AND GAO, J. 2013. Compact conformal map for greedy routing in wireless mobile sensor networks. In *INFOCOM*, IEEE, 2409–2417.
- LIPMAN, Y., AND FUNKHOUSER, T. 2009. Möbius voting for surface correspondence. *ACM Trans. Graph.* 28, 3 (July), 72:1–72:12.
- LIPMAN, Y. 2012. Bounded distortion mapping spaces for triangular meshes. *ACM Trans. Graph.* 31, 4 (July), 108:1–108:13.
- LIU, Y., POTTMANN, H., WALLNER, J., YANG, Y.-L., AND WANG, W. 2006. Geometric modeling with conical meshes and developable surfaces. *ACM Trans. Graph.* 25, 3 (July), 681–689.
- LUO, S.-J., YUE, Y., HUANG, C.-K., CHUNG, Y.-H., IMAI, S., NISHITA, T., AND CHEN, B.-Y. 2015. Legolization: Optimizing lego designs. *ACM Trans. Graph.* 34, 6 (Oct.), 222:1–222:12.
- MULLEN, P., TONG, Y., ALLIEZ, P., AND DESBRUN, M. 2008. Spectral conformal parameterization. *Computer Graphics Forum* 27, 5, 1487–1494.
- PÉREZ, J., THOMASZEWSKI, B., COROS, S., BICKEL, B., CANABAL, J. A., SUMNER, R., AND OTADUY, M. A. 2015. Design and fabrication of flexible rod meshes. *ACM Trans. Graph.* 34, 4 (July), 138:1–138:12.
- POTTMANN, H., EIGENSATZ, M., VAXMAN, A., AND WALLNER, J. 2015. Architectural geometry. *Computers & Graphics* 47, 145–164.
- RAFSANJANI, A., AND PASINI, D. 2016. Multistable compliant auxetic metamaterials inspired by geometric patterns in Islamic arts. APS March Meeting.
- RESCH, R. D. 1973. The topological design of sculptural and architectural systems. In *Proceedings of the June 4-8, 1973, National Computer Conference and Exposition*, ACM, New York, NY, USA, AFIPS '73, 643–650.
- RÖHRIG, T., SECHELMANN, S., KYCIA, A., AND FLEISCHMANN, M. 2014. Surface panelization using periodic conformal maps. In *Advances in Architectural Geometry 2014*. Springer International Publishing, 199–214.
- SCHIFTNER, A., HÖBINGER, M., WALLNER, J., AND POTTMANN, H. 2009. Packing circles and spheres on surfaces. *ACM Trans. Graph.* 28, 5 (Dec.), 139:1–139:8.
- SCHWARTZBURG, Y., AND PAULY, M. 2013. Fabrication-aware design with intersecting planar pieces. *Computer Graphics Forum* 32, 2, 317–326.
- SKOURAS, M., THOMASZEWSKI, B., KAUFMANN, P., GARG, A., BICKEL, B., GRINSPUN, E., AND GROSS, M. 2014. Designing inflatable structures. *ACM Trans. Graph.* 33, 4 (July), 63:1–63:10.
- SONG, P., FU, C.-W., GOSWAMI, P., ZHENG, J., MITRA, N. J., AND COHEN-OR, D. 2013. Reciprocal frame structures made easy. *ACM Trans. Graph.* 32, 4 (July), 94:1–94:13.
- SPRINGBORN, B., SCHRÖDER, P., AND PINKALL, U. 2008. Conformal equivalence of triangle meshes. *ACM Trans. Graph.* 27, 3 (Aug.), 77:1–77:11.
- STEPHENSON, K. 2003. Circle packing: a mathematical tale. *Notices of the AMS* 50, 11, 1376–1388.
- SULLIVAN, J. M. 2011. Conformal tiling on a torus. In *Proceedings of Bridges 2011: Mathematics, Music, Art, Architecture, Culture*, Tessellations Publishing, R. Sarhangi and C. H. Séquin, Eds., 593–596.
- TACHI, T. 2010. Origamizing polyhedral surfaces. *IEEE Trans. Vis. Comput. Graph.* 16, 2, 298–311.
- TACHI, T. 2013. Freeform origami tessellations by generalizing Resch's patterns. *Journal of Mechanical Design* 135, 11.
- TANG, C., BO, P., WALLNER, J., AND POTTMANN, H. 2016. Interactive design of developable surfaces. *ACM Trans. Graph.* 35, 2 (Jan.), 12:1–12:12.
- TESTUZ, R., SCHWARTZBURG, Y., AND PAULY, M. 2013. Automatic generation of constructable brick sculptures. In *Proc. Eurographics*.
- VAXMAN, A., MÜLLER, C., AND WEBER, O. 2015. Conformal mesh deformations with Möbius transformations. *ACM Trans. Graph.* 34, 4 (July), 55:1–55:11.
- WEBER, O., MYLES, A., AND ZORIN, D. 2012. Computing extremal quasiconformal maps. *Computer Graphics Forum* 31, 5, 1679–1689.
- ZIMMER, H., AND KOBELT, L. 2014. Zometool rationalization of freeform surfaces. *Visualization and Computer Graphics, IEEE Transactions on* 20, 10 (Oct), 1461–1473.

A Degrees of Freedom for a Trihexagonal Linkage

We here show that the number of degrees of freedom for a planar linkage is equal to the number of boundary vertices of degree 2, up to rigid motions. The basic idea is to start with the configuration space of each individual hexagon, then subtract the shared degrees of freedom. The rest is a rather tedious counting argument. Our main claim has also been validated via numerical experiment.

To begin, consider a disk-like subset of the trihexagonal tiling of the plane such that no boundary edge is contained in a hexagon—the collection of triangular faces in this subset corresponds to one of our linkages. Let V , E , and F denote the number of vertices, edges, and faces, and let $H := 2E$ denote the number of oriented edges or *halfedges*. Also let I and B denote the number of interior and boundary vertices (respectively), so that $V = I + B$, and let B_k denote the number of boundary vertices of degree k . Likewise, let F_k denote the number of faces of degree k , so that $F = F_3 + F_6$. The number of halfedges can then be expressed as $H = 3F_3 + 6F_6 + B$, i.e., we can associate three halfedges to each triangle, six to each hexagon, plus one more for each boundary edge.



Lemma 1. *The number of degree-2 and degree-4 boundary vertices is related by $B_4 = 2B_2 - 6$.*

Proof. For brevity, we will call degree-2 boundary vertices “black” and degree-4 boundary vertices “white.” Each black vertex can be uniquely identified with its two white neighbors ($+2B_2$), except where the polygon formed by the white vertices has a corner: at each convex corner one of the white vertices is shared (-1) and at each concave corner there is an additional white vertex ($+1$). Since the curve turns by $\pi/3$ at each corner and by 2π in total, the overall parity must be -6 . \square

Lemma 2. *The number of hexagons can be expressed as $F_6 = \frac{1}{2}F_3 - \frac{1}{3}B_2 - \frac{1}{12}(B_4 - 6)$.*

Proof. Triangulate each hexagon by inserting a vertex at its centroid; call original triangles “blue” and new triangles “green.” Each blue triangle is now adjacent to three green triangles ($+3F_3/6$), except along the boundary where blue triangles with a black vertex are adjacent to only one green triangle ($-2B_2/6$), and triangles with two white vertices are adjacent to only two green triangles ($(-B_4/2)/6$), modulo an adjustment -6 which arises for the same reason as in Lemma 1. \square

Lemma 3. $3F_6 - I = B_2 - 3$.

Proof. Recalling that $V = I + B$ we have $3F_6 - I = 3F_6 - V + B$, and applying Euler’s formula $V - E + F = 1$ for a disk, plus the fact that $H = 2E$ yields $3F_6 - (1 + E - F) + B = 3F_6 - 1 - H/2 + F + B$. Applying our earlier expression for H , this sum

becomes $F_6 - \frac{1}{2}F_3 + \frac{1}{2}B_4 + \frac{1}{2}B_2 - 1$. Applying Lemma 2 then yields $\frac{5}{12}B_4 + \frac{1}{6}B_2 - 1/2$, and applying Lemma 1 gives $B_2 - 3$, as desired. \square

Consider now that the motion of each hexagon can (independent of the rest of the linkage) be parameterized by its six exterior angles. Six quadratic constraints on edge length become 6 linear constraints on variations in position, leaving us with 3 angular degrees of freedom per hexagon (since angles specify a polygon only up to rigid motions). But since the angles around any interior vertex must sum to 2π , the linkage itself has only $3F_6 - I$ degrees of freedom—which we know from Lemma 3 is the same as $B_2 - 3$, i.e., a scalar value per degree-2 boundary vertex, up to a global rigid motion.

B Code for Non-penetration Constraint

Our numerical solver extends the open source implementation available at www.shapeop.org with the projection operator for the non-penetration constraint. Below is the code of our C++ implementation. Please refer to Section 4.2 for the definition of variables.

```
void NonPenetrationConstraint::project(
    const Matrix3X &positions, Matrix3X &projections
) const
{
    // Vertex indices
    int i0 = idI_[0], i1 = idI_[1],
        i2 = idI_[2], i3 = idI_[0];

    // Compute vectors v1, v2, v3
    Vector3 v1 = positions.col(i1) - positions.col(i0),
            v2 = positions.col(i2) - positions.col(i0),
            v3 = positions.col(i3) - positions.col(i0);

    // Compute the projections
    Vector3 proj1, proj2, proj3;

    // Verify the constraint
    if(v1.cross(v2).dot(v2.cross(v3)) < 0)
    {
        // Perform SVD to compute vector h
        Matrix32 M;
        M.col(0) = v2; M.col(1) = v3;
        JacobisVD<Matrix32> jsvd(M, ComputeFullU);
        Vector3 h = jsvd.matrixU().col(0);

        proj1 = v1;
        proj2 = h * h.dot(v2);
        proj3 = h * h.dot(v3);
    }
    else
    {
        proj1 = v1; proj2 = v2; proj3 = v3;
    }

    // Output the projection
    projections.col(idO_) = proj1;
    projections.col(idO_ + 1) = proj2;
    projections.col(idO_ + 2) = proj3;
}
```